Nano Energy 80 (2021) 105510

Contents lists available at ScienceDirect

Nano Energy

journal homepage: http://www.elsevier.com/locate/nanoen

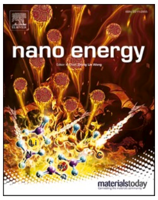

Full paper

Superstretchable, thermostable and ultrahigh-loading lithium–sulfur batteries based on nanostructural gel cathodes and gel electrolytes

Wen Yan, Jie Wei, Tao Chen, Lei Duan, Lei Wang, Xiaolan Xue, Renpeng Chen, Weihua Kong, Huinan Lin, Chenghui Li, Zhong Jin *

Key Laboratory of Mesoscopic Chemistry of MOE, Jiangsu Key Laboratory of Advanced Organic Materials, State Key Laboratory of Coordination Chemistry, School of Chemistry and Chemical Engineering, Nanjing University, Nanjing 210023, China

ARTICLE INFO

Keywords:
Lithium–sulfur batteries
Flexible and stretchable batteries
Gels
High sulfur loading
Thermostable

ABSTRACT

Lithium–sulfur batteries are desirable for portable and wearable electronic devices because of their high energy density, low cost and environmental friendliness. Herein, the fabrication of superstretchable Li–S batteries based on highly elastic gel cathodes (fracture strain: 1671%), gel electrolytes (fracture strain: 1223%), zigzag Cu wire-interconnected Li anode pieces and soft packages, is demonstrated. A phase inversion approach is developed to prepare gel cathodes composed of a homogeneously distributed 3D porous fluorinated copolymer skeleton, interlaced electron-conductive networks and sulfur-encapsulated hierarchical polar nanocomposites. The highly elastic gel cathodes possess tri-continuous structures with interpenetrated macropores favourable for high sulfur loading, electrolyte permeation and ion transport. The gel electrolytes with an amorphous phase copolymer matrix and tethered anions exhibit high ionic conductivity, thermal stability, flexibility and effective suppression of Li dendrite growth. The soft-packed Li–S batteries can be stretched up to 420% of their original length, function normally at 80 °C and deliver an ultrahigh areal capacity of 11.0 mAh cm^{-2} at a sulfur loading of 14 mg cm^{-2}.

1. Introduction

Flexible and stretchable energy storage systems are imperative for emerging portable and wearable electronic devices [1]. In contrast to the fabrication of conventional rigid secondary batteries, to fabricate flexible and stretchable batteries, all the functional components, including the cathode, anode, electrolyte/separator, current collector and package, should be redesigned and replaced with materials that can provide excellent stretchability and stable electrochemical performance [2–4]. Currently, the investigation of flexible and stretchable batteries mainly focuses on the design of battery configurations and the fabrication of stretchable electrodes that are compatible with Li-ion batteries [5–10]. However, the energy densities of Li-ion batteries are restrained by the low specific capacity and areal mass loading of the active materials [2]. Lithium–sulfur (Li–S) batteries are promising candidates for powering flexible and stretchable electronics owing to their high theoretical energy density (2597 Wh kg^{-1}), environmental friendliness and low cost [11]. To explore novel configuration designs and materials for the construction of flexible and stretchable Li–S batteries is very intriguing but remains a great challenge.

Numerous highly conductive carbonaceous materials [12–21] and porous polar inorganic nanomaterials [22–25] are promising sulfur hosts in Li–S batteries to accelerate the reaction kinetics of insulating elemental sulfur, and alleviate the shuttle effect of dissoluble intermediate lithium polysulfides (LiPSs) [26–28]. To improve the mechanical properties of sulfur composite cathodes, the coating or blending of polymer additives with carbonaceous sulfur host materials has been studied [11,28–37]. However, these reported sulfur composite cathodes could only accommodate low-level strains (e.g., a fracture strain ≤160%), which cannot satisfy the stretchability demands of flexible electronics used in kinetic environments. Moreover, with an increase in areal sulfur loading, the encapsulated sulfur is not easily accessible to the electrolyte, resulting in a limited utilization ratio. The rational design of flexible and stretchable cathode structures with high areal capacity, long cyclability and favourable elasticity still remains a challenging problem worth exploring. We suggest that the following desirable features are required: (1) a mechanically robust and stretchable electrode skeleton [28]; (2) a 3D-interpenetrated electron-conductive

---

* Corresponding author.
E-mail address: zhongjin@nju.edu.cn (Z. Jin).

https://doi.org/10.1016/j.nanoen.2020.105510
Received 9 September 2020; Received in revised form 10 October 2020; Accepted 13 October 2020

network throughout the electrode [1]; (3) an appropriate porosity to accommodate a large mass loading of sulfur and facilitate Li^+ ion transport during cycling [38]; and (4) effective inhibition of the shuttle effect of LiPSs [39,40]. Given that it is difficult to completely fulfil all of the above requirements with a single component, designing mechanically robust, lightweight composite cathodes consisting of multiple functional components is imperative for the construction of flexible and stretchable Li–S batteries without compromising the electrochemical performance under long-term operation and frequent mechanical deformation [28]. On the other hand, the design of a compatible electrolyte system is also crucial for the realization of flexible and stretchable batteries, but this is often overlooked. Gel electrolytes can provide much higher safety and better elasticity than a combination of conventional flammable liquid electrolytes and polypropylene (PP) separators. However, the application of gel electrolytes in fully stretchable batteries has not been sufficiently investigated [41–43]. Moreover, the modular design and rational selection of Li anodes, current collectors and elastic packages should also be thoughtfully considered to maintain the performance stability of entire integrated batteries under drastic types of deformation, such as bending, twisting and stretching [2,8].

Herein, we report the rational construction of superstretchable Li–S batteries based on highly elastic gel cathodes, gel electrolytes, wire-interconnected Li anode pieces and soft packages, as illustrated in Fig. 1a. Integrated 3D porous gel cathodes composed of a highly elastic fluorinated polymer matrix, polar sulfur reservoirs, and crosslinked multi-walled carbon nanotube (MWCNT) conductive networks were used as superstretchable and ultrahigh-sulfur gel cathodes (Fig. 1b). Via a phase inversion and swelling treatment process, a highly elastic gel based on poly(vinylidene fluoride-hexafluoropropylene) (PVdF-HFP) copolymer was fabricated and used as the 3D porous skeleton of the gel cathodes. Co nanoparticle-embedded N-doped carbon nanopolyhedra/N-doped carbon nanotube (Co@NCNP/NCNT) composites were used as the polar sulfur reservoirs; they have the merits of a hierarchical porous structure for accommodating the large volume of sulfur and intermediate LiPSs and have a strong affinity for the chemisorption of sulfur species to suppress the shuttle effect. Moreover, 3D-interlaced MWCNT networks were homogeneously distributed over the gel skeleton and intertwined with S@Co@NCNP/NCNT nanostructures to serve as highly conductive electron pathways. The PVdF-HFP/MWCNT gel framework is chemically stable and electrochemically stable at high voltage. Moreover, the abundant 3D-interconnected macropores in the conductive gel matrix can effectively facilitate the infiltration and transport of Li^+ ions during charge/discharge processes, thus ensuring high electrochemical kinetics and sulfur utilization. The as-obtained gel cathodes with the above functional components synergistically improve the mechanical and electrochemical performance and exhibit remarkable stretchability and long-term cycling capability even at a ultrahigh sulfur loading of 14 mg cm^{-2}. On the other hand, ionic liquid-immobilized polymer gel electrolyte with high ionic conductivity, favourable mechanical stretchability and good heat resistance were prepared and incorporated into flexible and stretchable Li–S batteries. Moreover, to provide high stretchability for the entire Li–S battery, modularized Li foil pieces connected by zigzag Cu wires were utilized as the anode, and highly elastic polymer membranes were used as the soft packages. In this way, superstretchable soft-packed Li–S batteries were assembled by combining the above prefabricated components, in which the gel cathode, gel electrolyte, wire-connected Li anode pieces and elastic packages can simultaneously provide favourable electrochemical functionalities as well as excellent mechanical stretchability (Fig. 1a). As a result, the soft-packed Li–S batteries can be stretched up to 420% of their original length and still maintain a stable electrochemical performance, thus fulfilling the diverse requirements of portable and wearable devices.

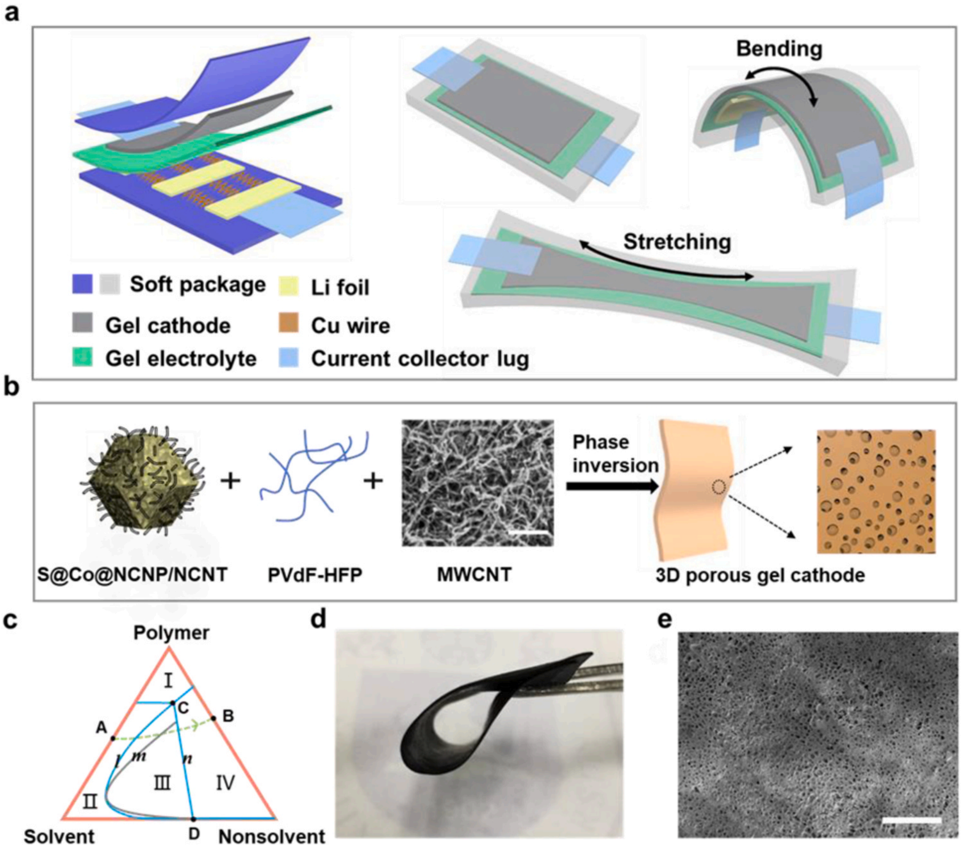

Fig. 1. Schematic configuration of superstretchable Li–S batteries and the preparation of 3D porous gel cathodes. (a) Assembly of superstretchable Li–S batteries with highly elastic composite gel cathodes, gel electrolytes, zigzag Cu wire-interconnected Li anode pieces and elastic packages. (b) Phase inversion strategy for fabricating a 3D porous gel cathode composed of sulfur-encapsulated and Co nanoparticle-embedded N-doped carbon nanopolyhedra/N-doped carbon nanotube composite (S@Co@NCNP/NCNT), poly(vinylidene fluoride-hexafluoropropylene) (PVdF-HFP) copolymer matrix and multi-walled carbon nanotube (MWCNT) conductive networks. Scale bar, 1 μm. (c) Phase diagram of the phase inversion process. I: Solid phase; II: Polymer solution single phase; III: Liquid-liquid dual phases; and IV: Solid-liquid dual phases. Route A to B: The process from polymer solution to gel membrane; Point C: Solidifying point; Point D: Critical gelation point; *l*: Bimodal line; *m*: Spinodal line; and *n*: Gelation boundary line. (d) Optical photograph (e) SEM image of the as-prepared 3D porous gel cathode. Scale bar, 50 μm.

2. Results and discussion

2.1. Fabrication and characterization of gel cathodes

As depicted in Fig. 1b, the superstretchable gel cathode was fabricated via a phase inversion approach, which is based on the mixing and phase separation of a polymer-solvent mixture and nonsolvent and is well-known for constructing porous polymer structures with 3D porous skeletons [44]. As illustrated in the phase diagram (Fig. 1c) from point A to B, when the polymer-solvent mixture is brought into contact with the nonsolvent, a nonsolvent-polymer-solvent intermediate is first formed and then two phases are formed: the polymer-rich phase and the polymer-lean phase, owing to the thermodynamic miscibility gap [45]. Finally, the polymer-rich phase solidifies to form the skeleton of the gel cathode, while the polymer-lean phase forms abundant pores in the gel membrane (Figs. 1d, 1e). To prepare a sulfur-containing gel cathode with good electrochemical and mechanical performance for Li–S batteries, the polymer matrix framework, sulfur host material, and conductive pathways should all be taken into account. Fluorinated copolymer PVdF-HFP with a high content of HFP (~30 wt%) was used as the cathode skeleton and provided good electrochemical stability, remarkable stretchability and excellent thermal stability. The Co@NCNP/NCNT composite was synthesized as the hybrid sulfur host material to facilitate the redox kinetics and inhibit the shuttle effect of the polysulfides. As shown in Fig. S1, the Co@NCNP/NCNT composite was synthesized via a scalable pyrolysis process of a zeolitic imidazolate framework (ZIF-67) precursor under a H_2/Ar atmosphere. The nitrogen adsorption-desorption isotherms and pore size distribution curves of the Co@NCNP/NCNT composite are shown in Fig. S2. The specific surface area of Co@NCNP/NCNT composite was calculated to be 281 $m^2\ g^{-1}$ through the Brunauer-Emmett-Teller (BET) method. The pore size distribution of the Co@NCNP/NCNT composite was analysed by the nonlocal density functional theory (NLDFT) method, revealing the existence of micropores with an average size of 1.3 nm and mesopores with an average size of 3.8 nm. The hierarchical pores in Co@NCNP/NCNT composites are beneficial for the accommodation of sulfur species and Li^+ ion transport. As shown in the scanning electron microscopy (SEM) and transmission electron microscopy (TEM) images of the Co@NCNP/NCNT composite (Fig. 2a-c), abundant NCNT were grown on the external surface of the Co@NCNP/NCNT composite due to the catalysis of Co nanoparticles during the pyrolysis process. The outstretched NCNT improved the electron conductance and the specific surface area for electrolyte infiltration. Furthermore, the embedded Co nanoparticles and doped N species in the carbon scaffold of the Co@NCNP/NCNT strongly immobilized polysulfides by chemical interaction and promoted the electrochemical redox reactions of the polysulfides, thus ensuring a good electrochemical performance by the sulfur composite cathodes [46]. After encapsulating elemental sulfur via a melt-diffusion method, the sulfur-containing composite is referred to as S@Co@NCNP/NCNT. Scanning-TEM (STEM) images and corresponding energy-dispersive X-ray (EDX) elemental maps of the Co@NCNP/NCNT and S@Co@NCNP/NCNT composites clearly confirmed the presence of evenly dispersed C, Co, N and S elements (Fig. S3 and Fig. S4).

The gel cathode, which was composed of a 3D porous polymer skeleton, sulfur host composite, and interlaced 3D conductive pathways, was fabricated via the phase inversion method. The slurry, which contained PVdF-HFP, S@Co@NCNP/NCNT, and MWCNT, was spread on a

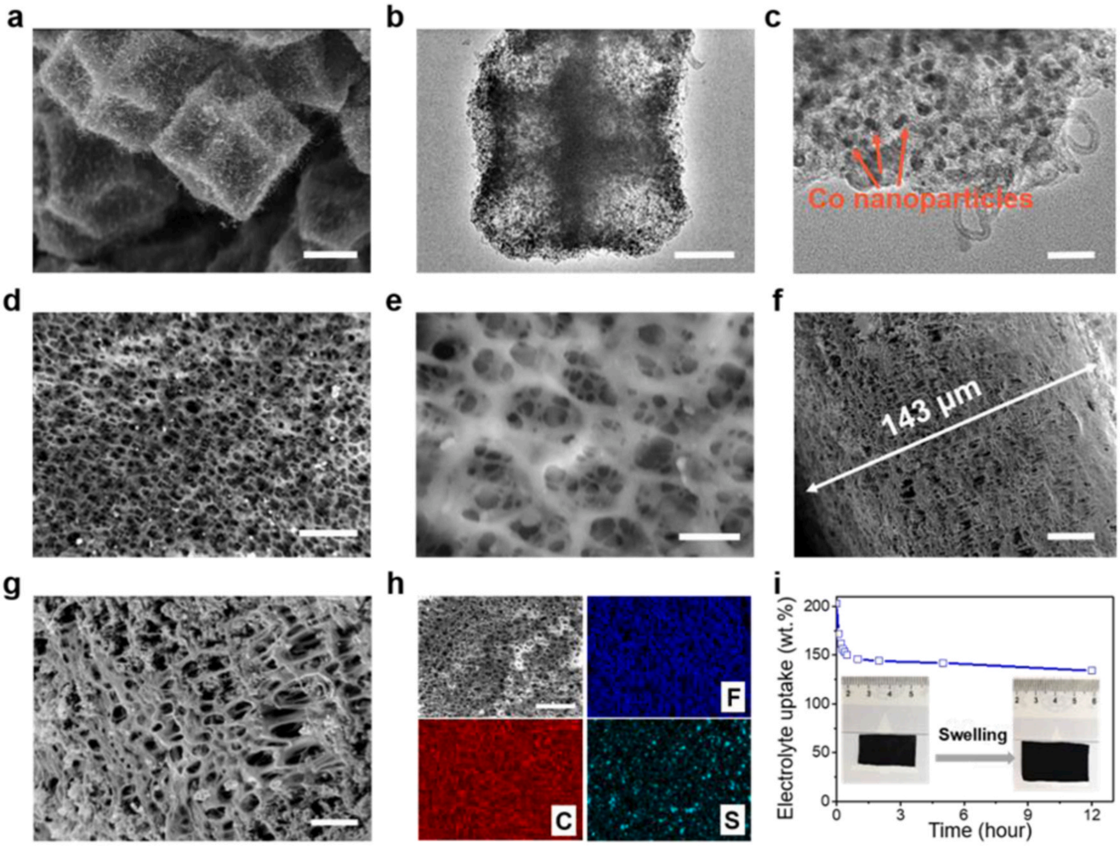

Fig. 2. Structural characterization of the sulfur host composite and 3D porous gel cathode. (a) SEM and (b and c) TEM images of Co@NCNP/NCNT composite used as the sulfur host. (d) and (e) Top-view SEM images of the gel cathode prepared by the phase inversion method. (f) and (g) Cross-section SEM image of the gel cathode. (h) Top-view SEM image of the gel cathode and the corresponding EDX maps of F, C and S. Scale bars: (a) 500 nm; (b) 300 nm; (c) 50 nm; (d) 5 μm; (e) 500 nm; (f) 20 μm; (g) 5 μm; and (h) 10 μm. (i) Electrolyte uptake of the gel cathode. The inset shows the swelling of the gel cathode after dipping in the LiTFSI solution for 30 min.

Petri dish and then immersed in deionized water. The phase inversion process of the slurry-water (nonsolvent) mixture quickly went from phase II to phase III and then to phase Ⅳ (Fig. 1c). The rapid gelation process of phase inversion is beneficial to the large-scale fabrication of gel cathodes. After drying, the gel cathode comprised a black, soft and highly elastic membrane (Fig. 1d). The polymer-rich phase consisted of three components: a continuous 3D porous PVdF-HFP skeleton, a crosslinked MWCNT conductive network and homogeneously dispersed S@Co@NCNP/NCNT particles, each of which performed their own functions in the gel cathode. Macropores with an average diameter of ~500 nm were formed due to the rapid interaction with the nonsolvent (by making contact with water during the phase inversion process), as shown in Figs. 2d, 2e. As shown in the cross-section SEM image (Fig. 2f, g), the gel cathode was ~143 μm thick and full of internal 3D-interconnected pores. The corresponding EDX maps of F, C and S elements confirmed the homogeneous distribution of the PVdF-HFP matrix, MWCNT and sulfur in the gel cathode (Fig. 2h). After immersion in the 1,2-dimethoxyethane/1,3-dioxolane (DME/DOL) solution of lithium bis (trifluoromethanesulfonyl)imide (LiTFSI), the gel cathode rapidly swelled into a 3D crosslinked structure with a sufficient amount of lithium salts reserved in the macropores and channels. The length and width of the gel cathode increased by 36%, and the thickness increased by 28% (Fig. 2i). The abundant macropores throughout the gel cathode led to an electrode density of 0.66 g cm^{-3}, a high porosity of 56%, and a high electrolyte uptake retention of 134 wt% after removal from the LiTFSI solution for 12 h. Moreover, the interlaced 3D MWCNT network incorporated into the 3D gel skeleton provided abundant connection with the S@Co@NCNP/NCNT loaded in the gel cathode and acted as an inner conductive network; these capabilities are superior to those of conventional metal current collectors than can only contact active materials on the surface. As illustrated in Fig. S5, the gel cathode with abundant 3D-interconnected macropores and channels rapidly swelled with a sufficient amount of lithium salts reserved (electrolyte uptake of 134 wt%), contributing to the high ion conductivity. Moreover, the S@Co@NCNP/NCNT and MWCNT components (50 wt% and 10 wt%, respectively) in the gel electrode have formed a conductive network in the electrode, and their volume fractions are high enough for the transport of electrons and lithium ions. The MWCNT network intertwined with S@Co@NCNP/NCNT also can serve as the current collector throughout the free-standing gel cathode without the need for a metal current collector. In this regard, the gel cathodes manufactured via the phase inversion method exhibited "tri-continuous" structures; that is, the stretchable 3D polymer skeletons contained an elastic matrix, abundant 3D-interconnected macropores as ion channels, and crosslinked MWCNT networks as electrically conductive pathways. Hence, the mechanical performance and electron/ion transport of the sulfur composite cathodes was greatly enhanced.

The crystallinity of the Co@NCNP/NCNT, S@Co@NCNP/NCNT, pristine PVdF-HFP gel and the as-prepared gel cathode were verified by X-ray diffraction (XRD), as shown in Fig. 3a. The XRD pattern of the Co@NCNP/NCNT composite shows three diffraction peaks at approximately 44.2°, 51.6°, and 75.9° that correspond to the (111), (200), and (220) lattice planes of the Co nanoparticles (JCPDS No. 89–4307) [47]. The same diffraction peaks are also shown in the XRD spectra for the S@Co@NCNP/NCNT composite and the gel cathode but with much lower intensities. The PVdF-HFP copolymer matrix exhibits semi-crystalline characteristics because of the modification of the amorphous HFP, thus providing a much better flexibility and stretchability than the pristine PVdF [48]. The reduced crystallinity also increases the number of pores that can accommodate the liquid electrolytes and promote Li$^+$ ion transport [49]. Moreover, the rigidity and elasticity of the gel cathode can be adjusted by controlling the ratio of the amorphous and crystalline phases because an increase in the amorphous phase ratio can improve the tensile strength [50,51]. Raman spectroscopy was conducted to investigate the carbonous surface compositions of the S@Co@NCNP/NCNT, MWCNT and the gel cathode Fig. 3b. The two prominent peaks at 1346 cm^{-1} (D band) and 1595 cm^{-1} (G band) were attributed to disordered/defective carbon and graphitic carbon, respectively. No obvious Raman peaks attributed to sulfur (generally located in the range from 300 to 500 cm^{-1}) were detected on the surface of the S@Co@NCNP/NCNT, indicating that elemental sulfur was well encapsulated by the Co@NCNP/NCNT [52]. The gel cathode only

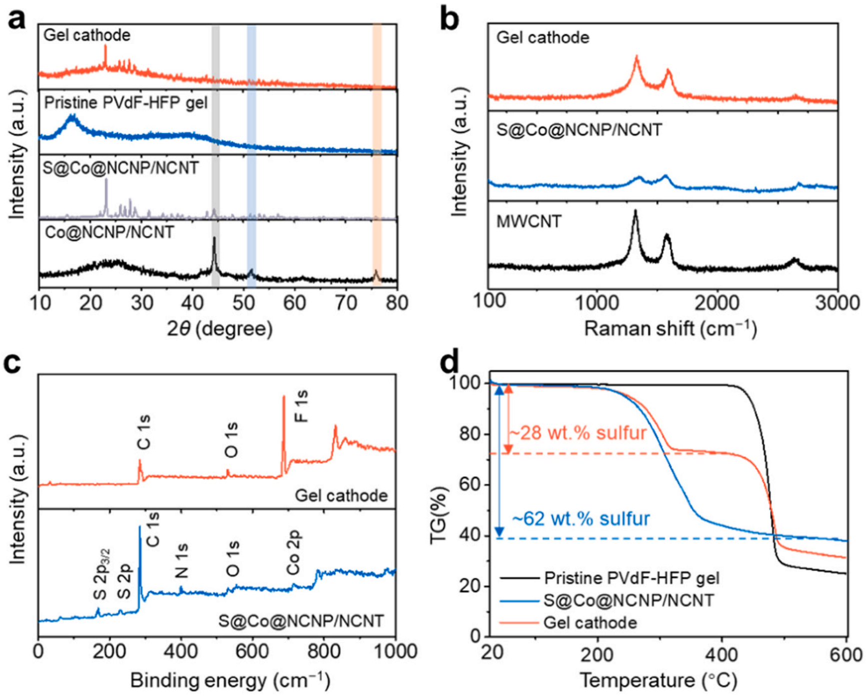

Fig. 3. Structural and Compositional characterizations. (a) XRD patterns of Co@NCNP/NCNT, S@Co@NCNP/NCNT, pristine PVdF-HFP gel and the as-prepared gel cathode. (b) Raman spectra of MWCNT, S@Co@NCNP/NCNT and the gel cathode. (c) XPS survey spectra of S@Co@NCNP/NCNT and the gel cathode. (d) TGA curves of pristine PVdF-HFP gel, S@Co@NCNP/NCNT and the gel cathode.

exhibited two Raman peaks that originated from the MWCNT network because the S@Co@NCNP/NCNT particles were wrapped by the MWCNT and PVdF-HFP, which is consistent with the SEM characterization Fig. 2d-h. Attenuated total reflection Fourier transform infrared (ATR-FTIR) spectra of the PVdF-HFP gel and the gel cathode are shown in Fig. S6. The characteristic bands at 1402 and 1180 cm^{-1} correspond to the C-H stretching vibration and the C-F stretching vibration of PVdF-HFP, respectively. The ATR-FTIR results also reveal the different phases of the polymer matrix. The bands at 1064, 976, 855, 795, 763, 613, and 532 cm^{-1} belong to the vibrations of the α phase, while the bands at 879 and 841 cm^{-1} belong to the vibrations of the β phase and γ phases, respectively, which are both often described as amorphous [53].

X-ray photoelectron spectroscopy (XPS) was conducted to analyse the surface chemical compositions of the S@Co@NCNP/NCNT and gel cathode Fig. 3c. The high-resolution XPS spectrum of the S@Co@NCNP/NCNT in the C 1s region contained two bands at 284.5 and 285.6 eV (Fig. S7a) corresponding to C=C and C=N bonds, respectively. The N 1s band of the S@Co@NCNP/NCNT can be deconvoluted into three peaks located at 398.6, 400.8, and 401.3 eV that correspond to pyridinic, pyrrolic, and graphitic N species, respectively (Fig. S7b). The Co $2p_{3/2}$ XPS spectrum exhibits two peaks at 778.5 and 780.3 eV (Fig. S7c) that correspond to metallic Co(0) and N coordinated Co^{2+} ($Co–N_x$), respectively [54,55]. The N and Co heteroatoms in carbon scaffolds are favourable for the binding of sulfur species and are beneficial for improving the long-term cycling stability and rate capability of Li–S batteries. The two peaks in the S 2p region at approximately 163.6 and 164.8 eV were assigned to S $2p_{3/2}$ and S $2p_{1/2}$, respectively, confirming the presence of S_8 molecules (Fig. S7d). The sulfur content of the S@Co@NCNP/NCNT measured by XPS was only 1.9 wt%, much lower than that measured by thermogravimetric analysis (TGA) analysis (Fig. 3d), suggesting that very little sulfur was deposited on the surface of the Co@NCNP/NCNT. XPS of the gel cathode was also conducted to confirm its surface state. Two discernible C 1s and F 1s peaks from the gel cathode were observed (Fig. 3c), and the C and F mole ratio was estimated to be 62:38, much larger than the mole ratio in pristine PVdF-HFP (5:8). The excess carbon indicates that the MWCNT were exposed to the surface of the gel cathode, which is consistent with the SEM and Raman results. Figure 3d shows two decomposition steps in the TGA of the gel cathode. First, elemental S in the S@Co@NCNP/NCNT started to evaporate at ~180 °C, and most of the S was evaporated by ~420 °C, revealing a sulfur loading ratio of 62 wt% in the S@Co@NCNP/NCNT. Second, the PVdF-HFP started to decompose at ~420 °C, and when the temperature reached 600 °C, ~30 wt% of residue remained. Therefore, the sulfur content in the whole gel cathode was calculated to be 28 wt%, confirming the fabrication of a lightweight and free-standing gel cathode without the need for a metal current collector.

2.2. Fabrication and characterizations of gel electrolyte

In addition to the gel cathode, another important component for superstretchable batteries is the electrolyte. In this work, a highly elastic gel electrolyte based on a 1-ethyl-3-methylimidazolium bis

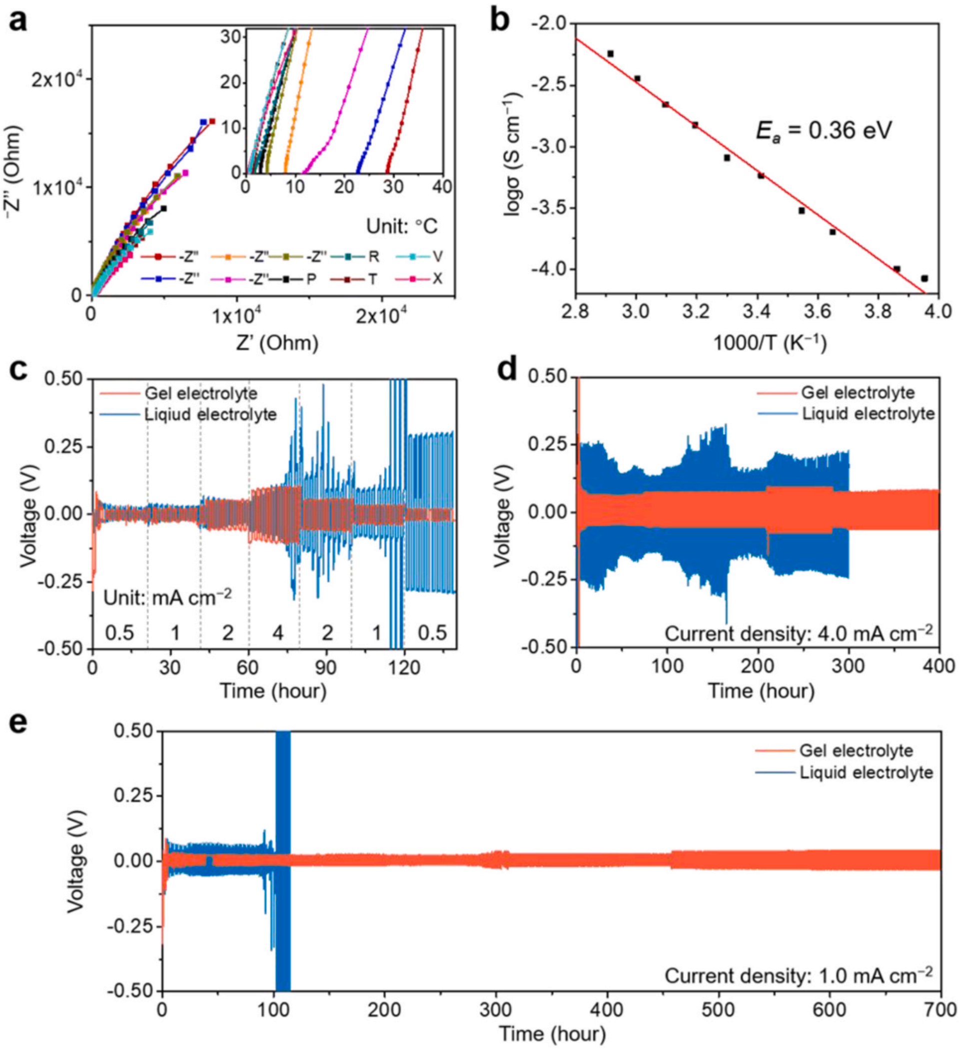

Fig. 4. Electrochemical performances of the gel electrolyte. (a) EIS profiles and (b) Arrhenius plot of the gel electrolyte at temperatures ranging from −20–70 °C. (c) Rate performance of the Li/Li symmetric cells assembled with the gel electrolyte and conventional DME/DOL-based liquid electrolyte-soaked PP separator at different current densities of 0.5, 1.0, 2.0 and 4.0 mA cm^{-2} for 1.0 h per plating/stripping. (d) Galvanostatic cycling profiles of Li/Li symmetric cells assembled with the gel electrolyte and conventional liquid electrolyte-soaked PP separator at 4.0 mA cm^{-2} for 4.0 mAh cm^{-2} per plating/stripping. (e) Galvanostatic cycling profiles of Li/Li symmetric cells assembled with the gel electrolyte and conventional liquid electrolyte-soaked PP separator at 1.0 mA cm^{-2} for 1.0 mAh cm^{-2} per plating/stripping.

(trifluoromethylsulfonyl)imide (EMI-TFSI) ionic liquid (IL)-immobilized PVdF-HFP copolymer (~30 wt% HFP) was proposed, which exhibits strong ion-dipole interactions between imidazolium-based IL and C–F dipoles that could ensure high Li^+ ion conductivity and effectively suppress Li dendrite growth. Electrochemical impedance spectroscopy (EIS) analysis was conducted to evaluate the Li^+ ion conductivity of the gel electrolyte (Fig. 4a). The ionic conductivities of the gel electrolyte at −20, −14, 1, 9, 20, 30, 40, 50, 60, and 70 °C were 8.4×10^{-5}, 1.0×10^{-4}, 2.0×10^{-4}, 3.0×10^{-4}, 5.8×10^{-4}, 8.1×10^{-4}, 1.5×10^{-3}, 2.2×10^{-3}, 3.6×10^{-3}, and 5.7×10^{-3} S cm^{-1}, respectively. The apparent activation energy (E_a) for ionic conduction was calculated to be 0.36 eV according to the slope of the Arrhenius plot (Fig. 4b and Table S1). The immobilized IL anions and the increased amorphous phase ratio of the gel electrolyte could guarantee rapid Li^+ ion conduction over a wide temperature range, resulting in higher ionic conductivity than the conventional DME/DOL-based liquid electrolyte-soaked PP separator (4.0×10^{-4} S cm^{-1} at 25 °C) [56]. The lithium ion transference numbers (t_{Li}^{+}) of the gel electrolyte and the liquid electrolyte-soaked PP separator were also evaluated, as shown in Fig. S8. The t_{Li}^{+} value of the gel electrolyte (0.53) is obviously higher than that of the liquid electrolyte-soaked PP separator (0.45), demonstrating that the fluorinated copolymer chain in the gel electrolyte can effectively immobilize the anions and inhibit the salt concentration gradients, which may limit the battery kinetics.

The electrochemical stability of the gel electrolyte was evaluated by the linear sweep voltammetry (LSV) method and showed a stable voltage window of 4.5 V vs. Li^+/Li (Fig. S9). To evaluate the compatibility of the gel electrolyte with the Li metal electrode, galvanostatic plating/stripping tests in Li/Li symmetric cells were performed. A stable Li deposition was achieved in the Li/Li symmetric cells assembled with the gel electrolyte (Fig. 4c). The voltage polarization of the gel electrolyte at current densities of 0.5, 1.0, 2.0, and 4.0 mA cm^{-2} were 0.02, 0.03, 0.05, and 0.09 V, respectively, indicating good capability of the gel electrolyte for stable Li stripping/plating. In contrast, the voltage polarization of Li/Li symmetric cells assembled with a conventional liquid electrolyte-soaked PP separator increased to 0.43 V at 4.0 mA cm^{-2}, showing that a short circuit was induced by Li dendrite growth. In Fig. 4d, when the Li/Li symmetric cell assembled with the gel electrolyte was cycled at 4.0 mA cm^{-2}, it exhibited a much smaller overpotential (0.09 V) and longer cycling stability (400 h) than that assembled with a conventional liquid electrolyte-soaked PP separator (0.26 V and 300 h). The long-term stability test of the gel electrolyte-based symmetric cell at 1.0 mA cm^{-2} exhibited excellent cyclability without any short circuits for 700 h (Fig. 4e). Fig. S10 shows the SEM images of the Li foils at fresh state and after plating/stripping at 1.0 mA cm^{-2} for 100 h. For the Li foils in the batteries assembled with DME/DOL-based liquid electrolyte-

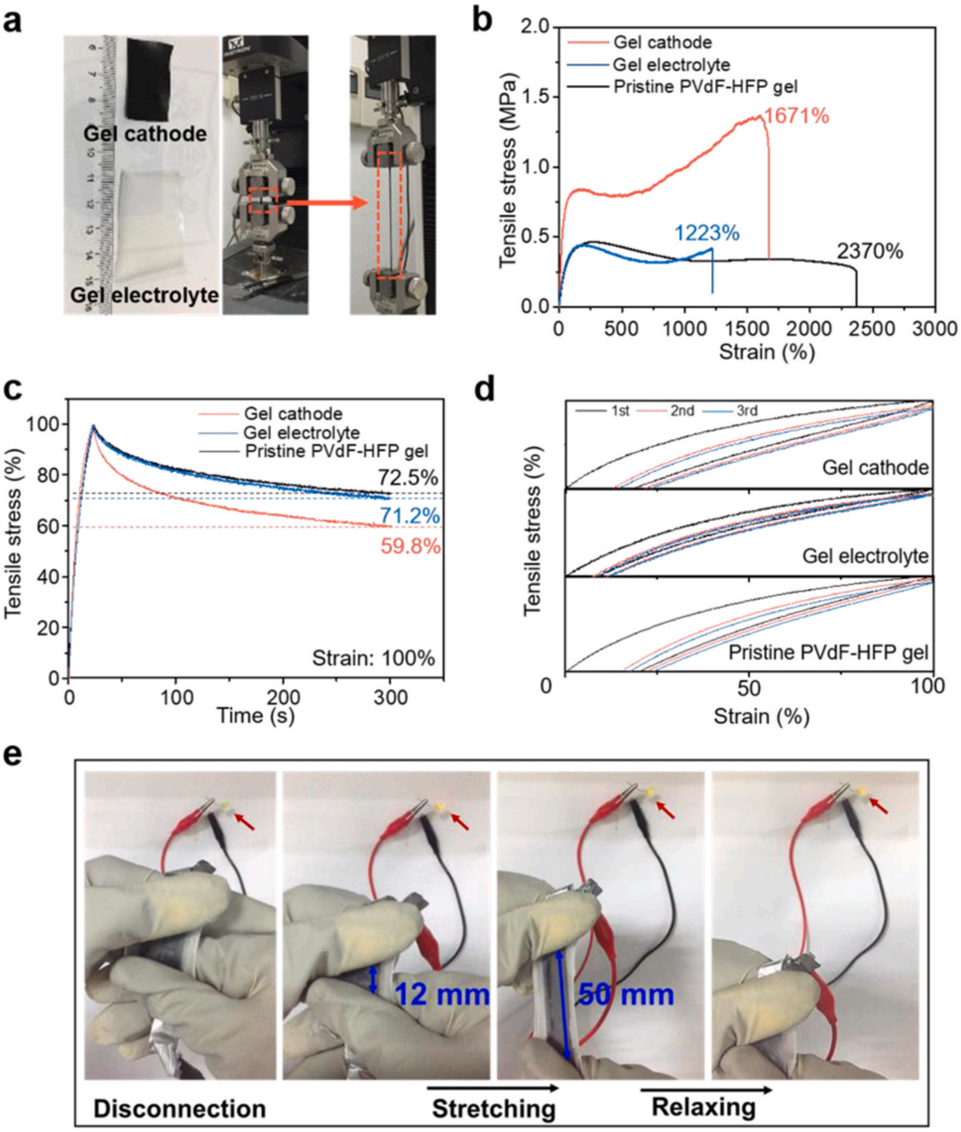

Fig. 5. Mechanical properties of the super-stretchable gel components and batteries. (a) Optical photograph of the gel cathode and gel electrolyte (left). Tensile test of the gel cathode sample under tensile test (right). (b) Stress-strain curves of the gel cathode, gel electrolyte, and pristine PVdF-HFP gel. (c) Stress relaxation curves and (d) stress-strain curves of the gel cathode, gel electrolyte, and pristine PVdF-HFP gel. (e) The as-prepared super-stretchable soft-packed Li–S battery lighting up a LED during continuous stretching-relaxing cycles by repeatedly stretching to 420% of its original length. The mass ratio of S@Co@NCNP/NCNT, MWCNT and PVdF-HFP in the gel cathode is 5:1:4.

soaked PP separator, the Li foil surface shows a rough and loose structure with appearance of micron-scale inactive lithium (Fig. S10c, d). In contrast, the Li foils in the batteries assembled with gel electrolyte remains flat and dense without Li dendrites and inactive Li (Fig. S10e, f). These results verify that the gel electrolyte could effectively suppress Li dendrite growth and ensure the long-term cycling ability of Li metal batteries, making it a promising candidate for stretchable batteries.

2.3. Mechanical properties of gel cathodes, gel electrolytes and stretchable batteries

To fabricate integrated superstretchable batteries, the mechanical performance of the key components should be determined. The stretchability of the gel cathode, gel electrolyte and pristine PVdF-HFP gel were measured by tensile experiments (Fig. 5a). As shown in Fig. 5b, the stress-strain curves consisted of an initial stiffening region (in which the tension significantly increased with increasing strain), followed by a subsequent steady region where the stress was almost constant until the membrane broke apart. An ultimate fracture strain of 1671% with a maximum tensile strength of 1.33 MPa and a Young's modulus of 2.74 MPa were achieved by the gel cathode with 40 wt% PVdF-HFP at a stretching rate of 10 mm min^{-1}. As control samples, the gel cathodes with higher sulfur contents were also prepared by increasing the mass ratio of S@Co@NCNP/NCNT to PVdF-HFP. The sulfur contents of the gel cathodes with 30 wt% and 20 wt% PVdF-HFP were calculated to be 39 wt% and 46 wt%, respectively. As shown in Fig. S11a, the ultimate fracture strain is 528% for the gel cathode with 30 wt% PVdF-HFP (maximum tensile strength: 3.17 MPa) and 206% for the gel cathode with 20 wt% PVdF-HFP (maximum tensile strength: 3.79 MPa), showing poorer stretchability than the gel cathode with 40 wt% PVdF-HFP (1671% with a maximum tensile strength of 1.33 MPa). Due to the rigidity of the sulfur composites, the gel cathodes with higher contents of S@Co@NCNP/NCNT exhibit larger Young's modulus of 5.90 MPa and 9.64 MPa. When the gel cathodes were strained at 100%, the tensile stress approached to 59.8%, 29.1% and 20.7%, respectively (Fig. 5c and Fig. S11b). Moreover, the stretching deformation of the gel cathode with the highest PVdF-HFP content has the smallest hysteresis (Fig. 5d and Fig. S11c, d), which are desirable mechanical properties for stretchable devices. The ultimate fracture strain of the gel electrolyte and the pristine PVdF-HFP gel were 1223% (maximum tensile strength: 0.45 MPa) and 2370% (maximum tensile strength: 0.46 MPa), respectively. When the gel electrolyte, and pristine PVdF-HFP gel were strained at 100%, the stress tensile curves decreased sharply and then approached 71.2% and 72.5%, respectively (Fig. 5c). When stretched and released for cycles, the gels showed self-recovery from the second cycle, which represented the elastic strain (Fig. 5d). To ensure the mechanical compatibility of the gel cathode, gel electrolyte and other key components in the superstretchable Li–S batteries, we utilized the gel cathode with relatively high PVdF-HFP content (40 wt%) in the batteries unless stated otherwise.

To verify the mechanical and electrochemical functionalities of the stretchable components, soft-packed Li–S batteries were assembled according to the structural configuration depicted in Fig. 1a. In a typical procedure, the gel electrolyte (4.5×2.5 cm^2) was sandwiched between the gel cathode (3×1.5 cm^2) and Cu wire-interconnected lithium foil pieces (1.5×0.5 cm^2 for each piece) and then sealed with PVdF-HFP film-based highly elastic soft packages (6×4 cm^2). As shown in Fig. 5e, the soft-packed Li–S battery was used to power up a light-emitting diode (LED) during continuous stretching-relaxing processes. The light intensity of the LED exhibited no visual disparity when the soft-packed battery was repeatedly stretched to 420% of its original length. Fig. S12 shows the electrochemical stability test of stretchable Li–S pouch cell under continuous stretching/releasing operation. The stretchable Li–S battery was tested upon continuous stretching−releasing operation at a maximum strain of ~80% for 50 cycles at 2.0 mA cm^{-2}. The discharge capacity reached 86% of the initial capacity after charging/discharging for 50 cycles, suggesting the high robustness and stable electrochemical performance of stretchable Li–S pouch cells under dynamic conditions. The soft-packed Li–S battery based on highly elastic gel components and PVdF-HFP packages exhibited a greatly improved stretchability compared with that of other reported configurations for flexible batteries [5,7,8,57].

2.4. Electrochemical performances

The electrochemical performance of the superstretchable Li–S batteries based on a gel cathode and gel electrolyte with 4 mg cm^{-2} areal sulfur loading were investigated (Fig. 6a). In the cyclic voltammetry (CV) curves, the reduction peaks at 2.26 V and 1.98 V (vs. Li/Li^+) were attributed to the lithiation of S_8 to intermediate polysulfides (Li_2S_x, $4 \leq x \leq 8$) and further to insoluble Li_2S or Li_2S_2 (Fig. 6a). The oxidation peak corresponds to the conversion process from Li_2S/Li_2S_2 to Li_2S_x ($4 \leq x \leq 8$) and eventually to S_8 [51]. The following CV cycles showed almost unchanged reduction/oxidation peak voltages and current densities, demonstrating high reversibility and effective suppression of electrochemical polarization. EIS was performed before and after CV analysis (Fig. S13a). The intercept at the Z′ real axis in the high-frequency region represents the contact resistance (R_0). The semicircle is related to the charge-transfer resistance during the redox reaction (R_{ct}), and the inclined line in the low-frequency region is associated with the Warburg impedance (W_0) [39]. After the CV test, the EIS curve transformed into a curve consisting of two semicircles in the middle-high frequency region. The semicircle at high-frequencies is associated with the aggregation of the Li_2S_2/Li_2S layer on the surface of the cathode (R_s), and the semicircle at the middle frequency is related to R_{ct}. The equivalent circuit model for the EIS curves is shown in Fig. S13b, c, and the corresponding resistances calculated from the equivalent circuit fitting are shown in Table S2. The gel cathode in the fresh cell exhibited an R_{ct} of 69.5 Ohm, indicating rapid charge transfer due to the favourable redox kinetics. After the CV test, the gel cathode exhibited an R_s of 10.5 Ohm and an R_{ct} of 10.7 Ohm, which is obviously lower than that of the fresh cell owing to the improved contact and ionic transport between the gel cathode and gel electrolyte.

The rate performance of the superstretchable Li–S battery is shown in Fig. 6b. In detail, the specific capacities at the current densities of 0.2 mA cm^{-2} (0.03 C, 1 C = 1675 mAh g^{-1}), 0.4 mA cm^{-2} (0.06 C), 0.6 mA cm^{-2} (0.09 C), 1.0 mA cm^{-2} (0.15 C) and 2.0 mA cm^{-2} (0.3 C) were 1156, 971, 857, 703 and 479 mAh g^{-1}, respectively. The specific capacity was restored to 1011 mAh g^{-1} when the current density returned to 0.2 mA cm^{-2}. Figure 6c shows the representative galvanostatic charge/discharge curves between 1.8 and 2.7 V at different current densities. At 0.2 mA cm^{-2}, the curves exhibited two discharging plateaus at 2.31 and 2.11 V and one charging plateau at 2.30 V. As the current density increased to 2.0 mA cm^{-2}, the discharging plateaus decreased to 2.23 and 1.92 V and the charging plateau increased to 2.38 V owing to the electrochemical polarization of the sulfur redox reactions. The Coulombic efficiency of the Li–S battery at 2.0 mA cm^{-2} approached 100%, suggesting that the shuttle effect of the LiPSs was effectively inhibited. As two control samples, the gel cathodes with different mass ratios of S@Co@NCNP/NCNT, MWCNT and PVdF-HFP (7:1:2 and 6:1:3) were also tested, showing discharge capacities of 611 and 517 mAh g^{-1} at 2.0 mA cm^{-2} (Fig. S14).

The gel electrolyte with PVdF-HFP matrix and IL additive shows excellent thermal stability due to the high degradation temperature of PVdF-HFP (>420 °C, Fig. 3d). On the other hand, the EMI-TFSI ionic liquid (IL) is reported to be capable of enduring remarkably high temperatures up to 400 °C [58], which is much higher than that of conventional mixed DME/DOL solvent (~80 °C). To further verify the thermal endurability of gel electrolyte boosted by PVdF-HFP and EMI-TFSI IL, the electrochemical performances of the Li–S batteries based on the gel electrolyte, the liquid electrolyte-soaked PP separator or the liquid electrolyte-soaked PVdF-HFP membrane (without the addition of

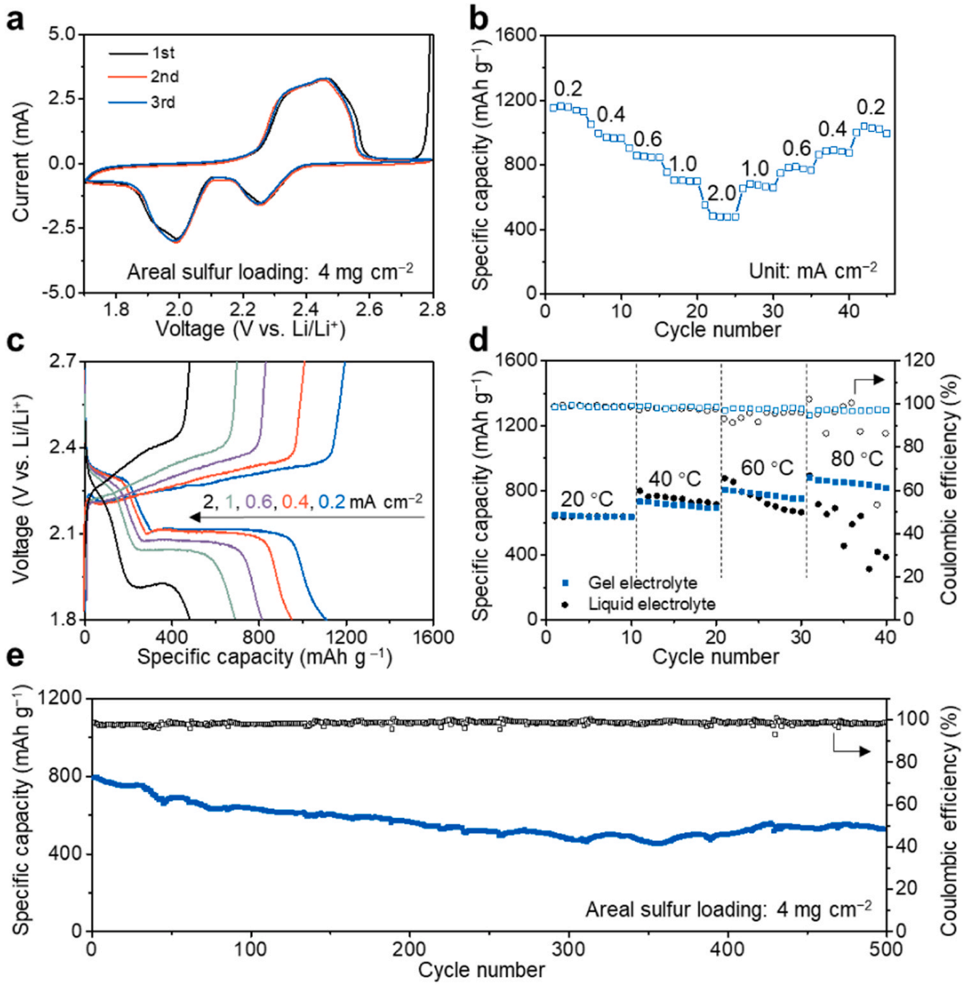

Fig. 6. Electrochemical performance of the superstretchable Li–S batteries. (a) CV curves of a superstretchable Li–S battery based on a gel cathode and gel electrolyte with an areal sulfur loading of 4 mg cm^{-2}. The scan rate was 0.02 mV s^{-1}. (b) Rate performance and (c) corresponding charge/discharge curves of the superstretchable Li–S battery at current densities from 0.2 to 2.0 mA cm^{-2}. (d) Specific capacities and Coulombic efficiencies of the Li–S batteries assembled with gel electrolyte or liquid electrolyte-soaked PP separator tested under various temperatures raised from 20 °C to 80 °C at 1.0 mA cm^{-2}. (e) Long-term cycling stability of the superstretchable Li–S battery at a current density of 2.0 mA cm^{-2}.

EMI-TFSI IL) were compared at high temperatures (Fig. 6d and Fig. S15). When the working temperature was raised from 20 °C to 80 °C, the Li–S battery assembled with the gel electrolyte exhibited the most stable capacities (815 mAh g^{-1}) and the highest Coulombic efficiencies (97.5%). Moreover, the result shows that the addition of EMI-TFSI IL is obviously helpful to the high temperature performance of Li–S batteries. Therefore, it can be concluded that the combined utilization of PVdF-HFP and IL could synergistically improve the thermal stability of the batteries. The Li–S batteries with the gel electrolyte also exhibit excellent rate capability at high temperature of 80 ℃ (Fig. S16). The discharge capacities are 1259, 1077, 983, 792 and 588 mAh g^{-1} with Coulombic efficiencies of 89.8%, 93.6%, 95.3%, 95.4% and 95.6% at 0.2, 0.4, 0.6, 1.0 and 2.0 mA cm^{-2}, respectively. When the current density decreases back to 0.2 mA cm^{-2}, the discharge capacity recovers back to a high level of 1138 mAh g^{-1}. In the long-term cycling test (Fig. 6e), the initial specific capacity was 792 mAh g^{-1} based on the sulfur loading mass (237 Ah kg^{-1} based on the total mass of the gel cathode). After 500 cycles, the reversible specific capacity remained at 555 mA h g^{-1} (166 Ah kg^{-1} based on the total mass of the gel cathode), corresponding to a low average capacity decay rate of 0.06% per cycle. As shown in Fig. S17a, a relatively smooth and dense surface of the Li foil anode can be maintained after long-term cycling, indicating a dendrite-free Li deposition morphology. Moreover, the morphology of gel cathode after cycling was also monitored by SEM (Fig. S17b), clearly showing that the porous architecture of the gel cathode is well preserved without significant damage. These results demonstrate that superstretchable Li–S batteries based on gel cathodes and gel electrolytes have a good rate capability and cycling stability.

The performance of the superstretchable Li–S batteries with higher sulfur loadings were measured (Fig. 7). The Li–S batteries based on gel cathodes with sulfur loadings of 4, 6, 10 and 14 mg cm^{-2} delivered reversible discharge capacities of 1350, 1230, 1000 and 941 mAh g^{-1} at 0.1 mA cm^{-2}, respectively, corresponding to 4.5, 6.2, 8.3 and 11.0 mAh cm^{-2}. When the current density increased to 2 mA cm^{-2}, the discharge capacities for sulfur loadings of 4, 6, 10 and 14 mg cm^{-2} were measured to be 829, 711, 598 and 530 mAh g^{-1}, respectively; after 50 cycles, the discharge capacities were well maintained at 708, 602, 462 and 412 mAh g^{-1} (with capacity retention of 86%, 85%, 78% and 78%), respectively, and the Coulombic efficiencies were approximately 92–99%. The EIS curves (Fig. 7b) indicated R_{ct} values of 71, 89, 129 and 210 Ohm for sulfur loadings of 4, 6, 10 and 14 mg cm^{-2}, respectively, confirming smooth electron and Li$^+$ ion transfer. The long-term cyclic performance of the superstretchable Li–S batteries with an ultrahigh areal sulfur loading of 14 mg cm^{-2} is shown in Fig. 7e, where a discharge capacity of 552 mAh g^{-1} was delivered (the specific capacity was 7.7 mAh cm^{-2} based on the cathode area or 364 mAh cm^{-3} based on the cathode volume). After 200 cycles, the discharge capacity was maintained at 350 mAh g^{-1} (4.9 mAh cm^{-2}) with a capacity decay of only 0.18% per cycle (0.44% per day). The charge/discharge profiles of the Li–S batteries with 14 mg cm^{-2} sulfur loading during the cycling process are displayed in Fig. S18, where the typical features of reversible conversion reactions between the S_8 and Li_2S_x species was retained. The as-prepared gel cathode showed a very competitive areal capacity among the reported polymer-containing sulfur composite cathodes (Figs. 7c, 7d) [11,28–30,32–35], and the stretchability was particularly excellent.

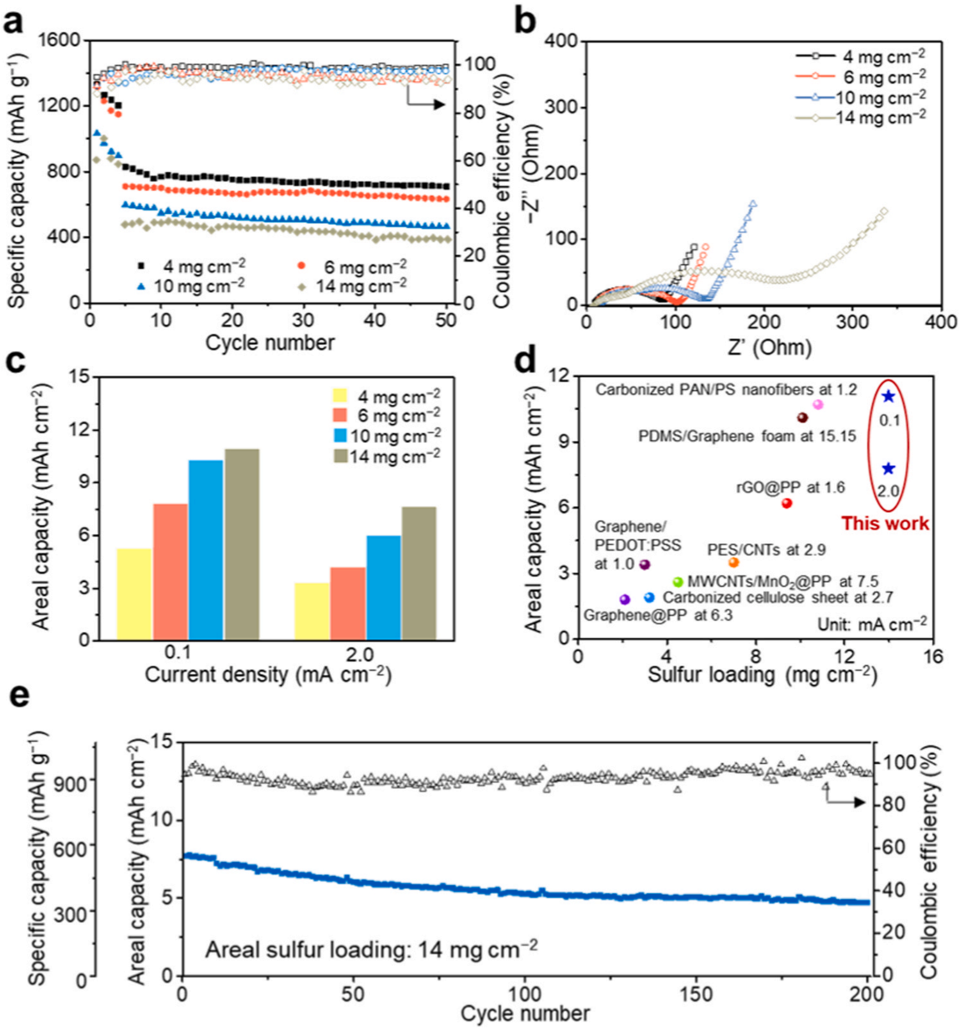

Fig. 7. Electrochemical performances of superstretchable Li–S batteries with ultrahigh sulfur loadings. (a) Capacity retention, (b) EIS curves and (c) bar diagrams of the areal capacities of superstretchable Li–S batteries with different sulfur loadings. The current density was 0.1 mA cm^{-2} for the initial 4 cycles and then held at 2.0 mA cm^{-2}. (d) Areal capacity and current density comparison of recently reported representative polymer-containing sulfur composite cathodes [11,28–30,32–35]. (e) Long-term cycling stability test of superstretchable Li–S batteries with an ultrahigh sulfur loading of 14 mg cm^{-2} at 2.0 mA cm^{-2}.

3. Conclusion

In summary, we developed superstretchable Li–S batteries in which all components are mechanically and electrochemically functional. Via a phase inversion strategy, highly elastic gel cathodes composed of a highly elastic PVdF-HFP skeleton, an interlaced MWCNT conductive network and homogeneously dispersed S@Co@NCNP/NCNT composites are constructed, exhibiting a remarkable ultimate fracture strain of 1671%. The as-obtained 3D-porous gel cathodes possess tri-continuous structures with interpenetrated macropores, which are favourable for high sulfur loading, electrolyte permeation and ion transport. On the other hand, gel electrolytes based on an amorphous phase fluorinated copolymer matrix and tethered anions with high ionic conductivity and thermal stability are optimized to obtain high elasticity (ultimate fracture strain: 1223%) for incorporation into superstretchable Li–S batteries. Zigzag Cu wire-interconnected Li anode pieces and PVdF-HFP membrane packages are also imperative for the fabrication of soft-packed Li–S batteries with outstanding stretchability (up to 420% of its original length). The superstretchable Li–S batteries with an ultrahigh sulfur loading up to 14 mg cm^{-2} deliver an areal capacity of 11.0 mAh cm^{-2} at 0.1 mA cm^{-2} and 7.7 mAh cm^{-2} at 2.0 mA cm^{-2}, maintaining 64% of its initial capacity after charging/discharging for 200 cycles. Further investigation on the improvement of high rate capability by exploring innovative materials and device structures with instinct conductivity and stretchability will be an important aspect of our future research. To further improve the rate performance and power density of the stretchable batteries, we suggest two promising strategies for further optimizing the gel cathode: (1) in-situ synthesis of stretchable and conductive polymer matrix in the well-designed carbonaceous/metallic framework; (2) the design and preparation of gelatinous nanostructures with excellent conductivity and stretchability via copolymerization and chemical modification. We suggest that integrating high-energy-density secondary batteries with superstretchable architecture can greatly boost the development of portable energy storage devices and wearable smart electronics.

4. Experimental section

4.1. Materials

All reagents were purchased from Sigma-Aldrich and used as received unless stated otherwise. MWCNT (TNM2, Timesnano) was purchased from Chengdu Organic Chemicals Co. Ltd. China. PVdF-HFP copolymer (with ~30 wt% of HFP) was synthesized and provided by Zhonghao Chenguang Chemical Industry Co., Ltd. China.

4.2. Preparation of the Co@NCNP/NCNT

The Co@NCNP/NCNT sulfur host material was obtained by pyrolysing ZIF-67. Briefly, 0.04 mol of 2-methylimidazole was dissolved in 200 mL of methanol and then quickly poured into 200 mL methanol solution of 0.05 M $Co(NO_3)_2$. After stirring for 1 min and resting for 24 h at room temperature, the ZIF-67 particles were collected by centrifugation, rinsed in ethanol several times, and then dried at 80 °C for 12 h. The ZIF-67 particles were heated to 350 °C and maintained at 350 °C for 1 h in a tube furnace under 100 sccm of Ar/H_2 flow (5 vol% H_2). Then, the above particles were further heated to 600 °C and maintained at 600 °C for 3 h under the same gas flow. The heating rate of the pyrolysis process is 2 °C min^{-1}. After cooling to room temperature naturally, the as-prepared products were treated in a mixed aqueous solution of 1 mol L^{-1} HCl and 0.5 mol L^{-1} $FeCl_3$ for 12 h to remove excess Co particles. The resulting samples were collected by centrifugation, repeatedly washed with water, and then dried at 80 °C overnight. The as-obtained black powders were designated Co@NCNP/NCNT.

4.3. Preparation of the sulfur-containing composites

The S@Co@NCNP/NCNT composites were fabricated via a melt-diffusion method. The sulfur composites were prepared by mixing sulfur power with Co@NCNP/NCNT with a weight ratio of 35:65. The mixtures were transferred to a sealed Teflon-lined autoclave, heated to 155 °C for 16 h and then cooled to room temperature.

4.4. Fabrication of the gel cathodes

The gel cathodes were prepared by a phase inversion method. Briefly, the S@Co@NCNP/NCNT, MWCNT and PVdF-HFP with mass ratios of 5:1:4, 6:1:3 and 7:1:2 were mixed in acetone for the preparation of gel cathodes with 40 wt%, 30 wt% and 20 wt% PVdF-HFP, respectively. The slurry was stirred for 4 h, poured into a Petri dish, and then immersed in deionized water for 1 min. After drying at 50 °C overnight, the gel cathode was cut into round disks with a diameter of 1.2 cm for coin cell tests. During the swelling process, the gel cathode was soaked in a solution containing 1.0 mol L^{-1} LiTFSI in 1,2-dimethoxyethane/1,3-dioxolane (DME/DOL) (1:1 in volume) with an additive of 1 wt% $LiNO_3$. The thicknesses of the gel cathodes were 143, 204, 338 and 511 μm for areal sulfur loadings of 4, 6, 10 and 14 mg cm^{-2}, respectively.

4.5. Fabrication of the gel electrolyte

The gel electrolyte was prepared with a high HFP content (~30 wt% HFP). Briefly, 1.0 g of PVdF-HFP and 0.4 g of 1-ethyl-3-methylimidazolium bis(trifluoromethylsulfonyl)imide (EMI-TFSI) IL were added to 10 mL of anhydrous acetone and vigorously stirred for 4 h. The resultant viscous solution was poured into a flat polytetrafluoroethylene (PTFE) mould and dried at 4 °C overnight to form a uniform IL-PVdF-HFP membrane with an area of 4 × 6 cm^2. The IL-PVdF-HFP membrane was then soaked in the solution (1.0 mol L^{-1} LiTFSI dissolved in a mixture of DME/DOL (1:1 in volume) with 1 wt% of $LiNO_3$ additive) for 20 min to form the gel electrolyte. The thickness of the gel electrolyte is measured to be 75 μm.

4.6. Material characterization

The samples were characterized with TEM (JEM-2100, operated at 120.0 kV) and field-emission SEM (FEI Nova NanoSEM 450) coupled with an attached EDX apparatus (Bruker Quantax-200). The sulfur loading mass was measured by TGA (Netzsch, STA 449 C) under N_2 flow at a heating rate of 10 °C min^{-1}. The powder XRD patterns were obtained using a Shimadzu XRD-6000 diffractometer with a Cu Kα radiation source (λ = 1.54178 Å). Raman spectroscopy analysis was performed on a Horiba JY Raman spectrometer using a 633 nm laser source. XPS analysis was conducted on a PHI-5000 Versa Probe X-ray photoelectron spectrometer using an Al Kα X-ray source. ATR-FTIR spectroscopy was performed on a Thermo Scientific NICOLET iS10 instrument. The tensile experiments were operated on an Instron 5565 instrument, and the gel films (4 mm wide and 0.2 mm thick) were stretched at a rate of 10 mm min^{-1}.

4.7. The porosity, density and electrolyte uptake of the gel cathodes

The porosity (p) and electrolyte uptake (e) of the gel cathodes were determined by the following equations [49]:

$$p = (m_{wet} - m_{dry}) / \rho S_{wet} T_{wet} \tag{1}$$

$$\rho_g = m_{dry} / v_{dry} \tag{2}$$

$$e = \frac{m_{wet} - m_{dry}}{m_{dry}} \times 100\% \tag{3}$$

where m_{dry} and m_{wet} are the weight of gel cathodes before and after immersion in the LiTFSI solution, respectively; ρ (1.117 g mL^{-1}) is the density of the LiTFSI solution; S_{wet} and T_{wet} are the area and thickness of the gel cathodes after immersion in the LiTFSI solution, respectively; and ρ_g and v_{dry} are the density and volume of the gel cathode, respectively.

4.8. Electrochemical measurements

All the batteries were assembled in an Ar-filled glove box. The Li/Li symmetric coin cells (CR2032 type) were assembled by sandwiching the gel electrolyte between two Li metal foils. The Li–S soft-packed batteries were assembled by sandwiching the gel electrolyte between Li metal foil pieces and the gel cathode, as depicted in Fig. 1a. Three pieces of Li metal foils (1.5 ×0.5 cm^2 for each piece) were adhered to zigzag Cu wires, serving as a stretchable anode. Al foils were used as current collector lugs for the cathode and anode. Two pieces of highly elastic PVdF-HFP film (6 × 4 cm^2) were used as the battery packages and sealed with epoxy resin. The CV and EIS curves were collected on a Chenhua CHI-760E electrochemical workstation. EIS measurements of Li−S cells and stainless steel/gel electrolyte/stainless steel cells were performed with an amplitude of 5 mV in the frequency ranges of 100 kHz–0.01 Hz and 1 MHz–1 Hz, respectively. The cycling and rate performances of Li/Li symmetric cells and Li–S cells were measured on a LAND CT2001A analyser. The specific capacities were calculated according to the sulfur loading mass in the cathodes unless stated otherwise.

CRediT authorship contribution statement

Wen Yan: Investigation, Writing - original draft. **Jie Wei:** Investigation. **Tao Chen:** Investigation. **Lei Duan:** Investigation. **Lei Wang:** Investigation. **Xiaolan Xue:** Investigation. **Renpeng Chen:** Investigation. **Weihua Kong:** Investigation. **Huinan Lin:** Investigation. **Chenghui Li:** Resources. **Zhong Jin:** Conceptualization, Supervision, Writing - review & editing.

Declaration of Competing Interest

The authors declare that they have no known competing financial interests or personal relationships that could have appeared to influence the work reported in this paper.

Acknowledgments

This work was supported by the National Key Research and Development Program of China (2017YFA0208200, 2016YFB0700600), the Fundamental Research Funds for the Central Universities (0205–14380219), the Projects of NSFC (21872069, 51761135104, 21573108), the Natural Science Foundation of Jiangsu Province (BK20180008), and the High-Level Innovation and Entrepreneurship Project of Jiangsu Province of China.

Author contributions

Z.J. conceived the idea of this study and designed the experiments. W.Y. performed the sample synthesis, electrochemical measurements and cell tests. W.Y., J.W., T.C., L.W., X.L.X., and H.N.L performed the material characterizations. W.Y., L.D., X.L.X, and R.P.C performed the tensile experiments. W.Y., T.C., W.H.K, R.P.C., C.H.L, and Z.J. analyzed the data and discussed the results. W.Y. wrote the manuscript. Z.J. revised the manuscript and supervised the project.

Data and Materials availability

The data that support the findings of this study are available from the corresponding author upon reasonable request.

Appendix A. Supporting information

Supplementary data associated with this article can be found in the online version at doi:10.1016/j.nanoen.2020.105510.

References

[1] G.M. Zhou, F. Li, H.M. Cheng, Progress in flexible lithium batteries and future prospects, Energy Environ. Sci. 7 (2014) 1307–1338.
[2] W. Liu, M.S. Song, B. Kong, Y. Cui, Adv. Mater. 29 (2017), 1603436.
[3] W.J. Song, S. Yoo, G. Song, S. Lee, M. Kong, J. Rim, U. Jeong, S. Park, Recent Progress in Stretchable Batteries for Wearable Electronics, Batter. Supercaps 2 (2019) 181–199.
[4] B. He, P. Man, Q. Zhang, H. Fu, Z. Zhou, C. Li, Q. Li, L. Wei, Y. Yao, All binder-free electrodes for high-performance wearable aqueous rechargeable sodium-ion batteries, Nano Micro Lett. 11 (2019) 101.
[5] S. Xu, Y. Zhang, J. Cho, J. Lee, X. Huang, L. Jia, J.A. Fan, Y. Su, J. Su, H. Zhang, H. Cheng, B. Lu, C. Yu, C. Chuang, T. Kim, T. Song, K. Shigeta, S. Kang, C. Dagdeviren, I. Petrov, P.V. Braun, Y. Huang, U. Paik, J.A. Rogers, Stretchable batteries with self-similar serpentine interconnects and integrated wireless recharging systems, Nat. Commun. 4 (2013) 1543.
[6] Z. Song, T. Ma, R. Tang, Q. Cheng, X. Wang, D. Krishnaraju, R. Panat, C.K. Chan, H. Yu, H. Jiang, Origami lithium-ion batteries, Nat. Commun. 5 (2014) 3140.
[7] W. Weng, Q. Sun, Y. Zhang, S. He, Q. Wu, J. Deng, X. Fang, G. Guan, J. Ren, H. Peng, A gum-like lithium-ion battery based on a novel arched structure, Adv. Mater. 27 (2015) 1363–1369.
[8] X. Chen, H. Huang, L. Pan, T. Liu, M. Niederberger, Cancer immunotherapy: massively evoking immunogenic cell death by focused mitochondrial oxidative stress using an AIE luminogen with a twisted molecular structure (Adv. Mater. 52/2019), Adv. Mater. 31 (2019), 1904648.
[9] Y. Sun, J. Lopez, H.W. Lee, N. Liu, G. Zheng, C.L. Wu, J. Sun, W. Liu, J.W. Chung, Z. Bao, Y. Cui, A stretchable graphitic carbon/Si anode enabled by conformal coating of a self-healing elastic polymer, Adv. Mater. 28 (2016) 2455–2461.
[10] M. Gu, W.J. Song, J. Hong, S.Y. Kim, T.J. Shin, N.A. Kotov, S. Park, B.S. Kim, Sci. Adv. 5 (2019), eaaw1879.
[11] Z. Li, J.T. Zhang, Y.M. Chen, J. Li, X.W. Lou, Pie-like electrode design for high-energy density lithium–sulfur batteries, Nat. Commun. 6 (2015) 8850.
[12] R. Elazari, G. Salitra, A. Garsuch, A. Panchenko, D. Aurbach, Sulfur-impregnated activated carbon fiber cloth as a binder-free cathode for rechargeable Li-S batteries, Adv. Mater. 23 (2011) 5641–5644.
[13] C. Zu, Y. Fu, A. Manthiram, Highly reversible Li/dissolved polysulfide batteries with binder-free carbon nanofiber electrodes, J. Mater. Chem. A 1 (2013) 10362.
[14] Y. Su, Y. Fu, A. Manthiram, Self-weaving sulfur–carbon composite cathodes for high rate lithium–sulfur batteries, Phys. Chem. Chem. Phys. 14 (2012) 14495–14499.
[15] G. Zhou, D.W. Wang, F. Li, P.X. Hou, L. Yin, C. Liu, G.Q. Lu, I.R. Gentle, H. M. Cheng, Energy Environ. Sci. 5 (2012) 8901–8906.
[16] Y. Fu, Y. Su, A. Manthiram, Highly reversible lithium/dissolved polysulfide batteries with carbon nanotube electrodes, Angew. Chem. Int. Ed. 52 (2013) 6930–6935.
[17] J. Jin, Z. Wen, G. Ma, Y. Lu, Y. Cui, M. Wu, X. Liang, X. Wu, RSC Adv. 3 (2013) 2558–2560.
[18] G. Zhou, L.C. Yin, D.W. Wang, L. Li, S. Pei, I.R. Gentle, F. Li, H.M. Cheng, ACS Nano 7 (2013) 5367–5375.
[19] M. Hagen, S. Dörfler, P. Fanz, T. Berger, R. Speck, J. Tübke, H. Althues, M. J. Hoffmann, C. Scherr, S. Kaskel, J. Power, Development and costs calculation of lithium–sulfur cells with high sulfur load and binder free electrodes, Sources 224 (2013) 260–268.
[20] S. Thieme, J. Brückner, I. Bauer, M. Oschatz, L. Borchardt, H. Althuesa, S. Kaskel, High capacity micro-mesoporous carbon–sulfur nanocomposite cathodes with enhanced cycling stability prepared by a solvent-free procedure, J. Mater. Chem. A 1 (2013) 9225–9234.
[21] L. Li, L. Hou, J. Cheng, T. Simmons, F. Zhang, L.T. Zhang, R.J. Linhardt, N. Koratkar, A flexible carbon/sulfur-cellulose core-shell structure for advanced lithium–sulfur batteries, Energy Storage Mater. 15 (2018) 388–395.
[22] G. Zhou, E. Paek, G.S. Hwang, A. Manthiram, Long-life Li/polysulphide batteries with high sulphur loading enabled by lightweight three-dimensional nitrogen/sulphur-codoped graphene sponge, Nat. Commun. 6 (2015) 7760.
[23] J. Chang, J. Shang, Y. Sun, L.K. Ono, D. Wang, Z. Ma, Q. Huang, D. Chen, G. Liu, Y. Cui, Y. Qi, Z. Zheng, Flexible and stable high-energy lithium-sulfur full batteries with only 100% oversized lithium, Nat. Commun. 9 (2018) 4480.
[24] X. Han, Y. Xu, X. Chen, Y.C. Chen, N. Weadock, J. Wan, H. Zhu, Y. Liu, H. Li, G. Rubloff, C. Wang, L. Hu, Reactivation of dissolved polysulfides in Li–S batteries based on atomic layer deposition of Al2O3 in nanoporous carbon cloth, Nano Energy 2 (2013) 1197–1206.
[25] L. Ma, W. Zhang, L. Wang, Y. Hu, G. Zhu, Y. Wang, R. Chen, T. Chen, Z. Tie, J. Liu, Z. Jin, ACS Nano 12 (2018) 4868–4876.
[26] Q. Pang, X. Liang, C.Y. Kwok, L.F. Nazar, Advances in lithium–sulfur batteries based on multifunctional cathodes and electrolytes, Nat. Energy 1 (2016) 16132.
[27] X. Liu, J. Huang, Q. Zhang, L. Mai, Adv. Mater. 29 (2017), 1601759.
[28] P. Xiao, F. Bu, G. Yang, Y. Zhang, Y. Xu, Adv. Mater. 29 (2017), 1703324.
[29] G. Zhou, L. Li, D.W. Wang, X. Shan, S. Pei, F. Li, H.M. Cheng, A flexible sulfur-graphene-polypropylene separator integrated electrode for advanced Li-S batteries, Adv. Mater. 27 (2015) 641–647.
[30] G. Zhou, L. Li, C. Ma, S. Wang, Y. Shi, N. Koratkar, W. Ren, F. Li, H.M. Cheng, A graphene foam electrode with high sulfur loading for flexible and high energy Li-S batteries, Nano Energy 11 (2015) 356–365.
[31] X. Fang, W. Weng, J. Ren, H. Peng, A cable-shaped lithium sulfur battery, Adv. Mater. 28 (2016) 491–496.
[32] F. Wu, E. Zhao, D. Gordon, Y. Xiao, C. Hu, G. Yushin, Infiltrated porous polymer sheets as free-standing flexible lithium-sulfur battery electrodes, Adv. Mater. 28 (2016) 6365–6371.
[33] M. Yao, R. Wang, Z. Zhao, Y. Liu, Z. Niu, J. Chen, ACS Nano 12 (2018) 12503–12511.
[34] W. Wahyudi, Z. Cao, P. Kumar, M. Li, Y. Wu, M.N. Hedhili, T.D. Anthopoulos, L. Cavallo, L.J. Li, J. Ming, Phase inversion strategy to flexible freestanding electrode: critical coupling of binders and electrolytes for high performance Li-S battery, Adv. Funct. Mater. 28 (2018), 1802244.
[35] H. Shi, S. Niu, W. Lv, G. Zhou, C. Zhang, Z. Sun, F. Li, F. Kang, Q.H. Yang, Easy fabrication of flexible and multilayer nanocarbon-based cathodes with a high unreal sulfur loading by electrostatic spraying for lithium-sulfur batteries, Carbon 138 (2018) 18–25.
[36] L. Miao, W. Wang, K. Yuan, Y. Yang, A. Wang, A lithium–sulfur cathode with high sulfur loading and high capacity per area: a binder-free carbon fiber cloth–sulfur material, Chem. Commun. 50 (2014) 13231–13234.
[37] S. Lu, Y. Chen, X. Wu, Z. Wang, Y. Li, Three-Dimensional sulfur/graphene multifunctional hybrid sponges for lithium-sulfur batteries with large areal mass loading, Sci. Rep. 4 (2014) 4629.
[38] Y. Mao, G. Li, Y. Guo, Z. Li, C. Liang, X. Peng, Z. Lin, Foldable interpenetrated metal-organic frameworks/carbon nanotubes thin film for lithium–sulfur batteries, Nat. Commun. 8 (2017) 14628.
[39] C.Y. Chen, H.J. Peng, T.Z. Hou, P.Y. Zhai, B.Q. Li, C. Tang, W. Zhu, J.Q. Wang, Q. Zhang, Adv. Mater. 29 (2017), 1606802.
[40] M. Yu, Z. Wang, Y. Wang, Y. Dong, J. Qiu, Adv. Energy Mater. 7 (2017), 1700018.
[41] Y. Wang, B. Li, J. Ji, A. Eyler, W. Zhong, A gum-like electrolyte: safety of a solid, performance of a liquid, Adv. Energy Mater. 3 (2013) 1557–1562.
[42] S. Choudhury, T. Saha, K. Naskar, M. Stamm, G. Heinrich, A. Das, A highly stretchable gel-polymer electrolyte for lithium-sulfur batteries, Polymer 112 (2017) 447–456.
[43] J. Guan, Y. Li, J. Li, Stretchable ionic-liquid-based gel polymer electrolytes for lithium-ion batteries, Ind. Eng. Chem. Res. 56 (2017) 12456–12463.
[44] F. Liu, N.A. Hashim, Y. Liu, M.R.M. Abed, K. Li, Progress in the production and modification of PVDF membranes, J. Membr. Sci. 375 (2011) 1–27.
[45] H.H. Manuel, N. Ulrich, Modeling of pore formation in phase inversion processes: model and numerical results, J. Membr. Sci. 564 (2018) 820–831.
[46] Y. Li, J. Fan, M. Zheng, Q. Dong, A novel synergistic composite with multi-functional effects for high-performance Li–S batteries, Energy Environ. Sci. 9 (2016) 1998–2004.
[47] Z. Li, C. Li, X. Ge, J. Ma, Z. Zhang, Q. Li, C. Wang, L. Yin, Reduced graphene oxide wrapped MOFs-derived cobalt-doped porous carbon polyhedrons as sulfur immobilizers as cathodes for high performance lithium sulfur batteries, Nano Energy 23 (2016) 15–26.
[48] R. Miao, B. Liu, Z. Zhu, Y. Liu, J. Li, X. Wang, Q. Li, J. Power, PVDF-HFP-based porous polymer electrolyte membranes for lithium-ion batteries, Sources 184 (2008) 420–426.

[49] J. Cao, B. Zhu, Y. Xu, Structure and ionic conductivity of porous polymer electrolytes based on PVDF-HFP copolymer membranes, J. Membr. Sci. 281 (2006) 446–453.

[50] Y. Cao, T.G. Morrissey, E. Acome, S.I. Allec, B.M. Wong, C. keplinger, C. Wang, Adv. Mater. 29 (2017), 1605099.

[51] X. Huang, Z. Huang, J.C. Lai, L. Li, G.C. Yang, C.H. Li, Self-healing improves the stability and safety of polymer bonded explosives, Compos. Sci. Technol. 167 (2018) 346–354.

[52] J. Guo, J. Zhang, F. Jiang, S. Zhao, Q. Su, G. Du, Microporous carbon nanosheets derived from corncobs for lithium–sulfur batteries, Electrochim. Acta 176 (2015) 853–860.

[53] S. Jeschke, M. Mutke, Z. Jiang, B. Alt, H.D. Wiemhöfer, ChemPhysChem 15 (2014) 1761–1771.

[54] S. Liu, Z. Wang, S. Zhou, F. Yu, M. Yu, C.-Y. Chiang, W. Zhou, J. Zhao, J. Qiu, Adv. Mater. 29 (2017), 1700874.

[55] W. Gong, Y. Lin, C. Chen, M.A.- Mamun, H.-S. Lu, G. Wang, H. Zhang, H. Zhao, Adv. Mater. 31 (2019), 1808341.

[56] J. Shim, H.J. Kim, B.G. Kim, Y.S. Kim, D.G. Kim, J.C. Lee, Energy Environ. Sci. 10 (2017) 1911–1916.

[57] J. Ren, Y. Zhang, W. Bai, X. Chen, Z. Zhang, X. Fang, W. Weng, Y. Wang, H. Peng, Elastic and wearable wire-shaped lithium-ion battery with high electrochemical performance, Angew. Chem. Int. Ed. 53 (2014) 7864–7869.

[58] H. Nakajima, H. Ohno, Preparation of thermally stable polymer electrolytes from imidazolium-type ionic liquid derivatives, Polymer 46 (2005) 11499–11504.

Wen Yan received her B.S. degree from Nanjing University in 2016. She is now pursuing her Ph.D. degree under the supervision of Prof. Zhong Jin in School of Chemistry and Chemical Engineering at Nanjing University. Her research interest focuses on the application of functional polymers in energy conversion and storage devices.

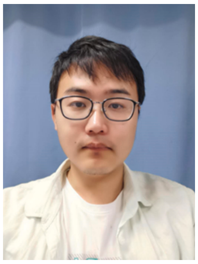

Jie Wei received his B.S. degree in Applied Chemistry from Hunan University in 2018. He is now pursuing his Ph.D. under the supervision of Prof. Zhong Jin in School of Chemistry and Chemical Engineering at Nanjing University. His research interest is mainly concentrated on redox flow batteries and lithium ion batteries.

Tao Chen received his Ph.D. degree in Chemical Engineering and Technology at Nanjing University of Science and Technology in June 2015. He worked as a postdoctoral scholar at Nanjing University in the group of Prof. Zhong Jin (2015–2019). His research focuses on the design and synthesis of nanostructured electrode materials for rechargeable batteries.

Lei Duan received his Ph.D. (2020) in School of Chemistry and Chemical Engineering, Nanjing University, P.R. China. His main interest is the design and fabrication of self-healing polymer materials and dielectric materials.

Lei Wang received his B.S. degree in Jiangsu University. He is now pursing his M.S. degree under the supervision of Prof. Zhong Jin in School of Chemistry and Chemical Engineering, Nanjing University. His main interest is the design of multivalent secondary batteries.

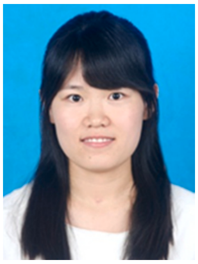

Xiaolan Xue received her B.S. degree in School of Chemistry and Chemical Engineering from Shannxi Normal University (2015). She is now pursing her Ph.D. degree under the supervision of Prof. Zhong Jin in School of Chemistry and Chemical Engineering, Nanjing University, P.R. China. Her research is focused on designing functional materials for rechargeable batteries.

Renpeng Chen graduated from the Northeastern University (2014). He is pursuing his Ph.D. degree under the guidance of Prof. Zhong Jin in School of Chemistry and Chemical Engineering at Nanjing University. His research interest is focused on the synthesis of alloy materials for lithium-ion batteries.

Weihua Kong received his B.S. degree from Hunan University in 2017. He is now pursuing his M.S degree under the supervision of Prof. Zhong Jin in School of Chemistry and Chemical Engineering at Nanjing University. His research interest is mainly concentrated on the lithium-sulfur and lithium-metal batteries.

Huinan Lin received her B.S. degree from Zhengzhou University in 2017. She is now pursuing her M.S degree under the supervision of Prof. Zhong Jin in School of Chemistry and Chemical Engineering at Nanjing University. Her research interest is lithium-metal batteries.

Prof. Chenghui Li received his B.S. degree (2002) from Nanchang University and Ph.D. degree (2007) from Nanjing University. He worked as a research assistant in the University of Hong Kong (Prof. Chi-Ming Che's group) in 2008. In 2013, he worked as a visiting scholar in Stanford University (Prof. Zhenan Bao's group). He is currently a Professor in School of Chemistry and Chemical Engineering, at Nanjing University. His current research focuses on the design and application of self-healing polymers.

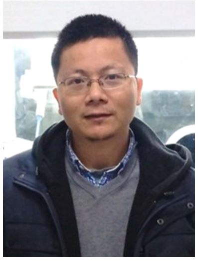

Prof. Zhong Jin received his B.S. (2003) and Ph.D. (2008) from Peking University. He worked as a postdoctoral scholar at Rice University (2008–2010) and Massachusetts Institute of Technology (2010–2014). He is currently a professor in School of Chemistry and Chemical Engineering at Nanjing University. Now he is leading a research group working on the design and development of advanced materials and device systems for clean energy conversion and storage.